

# An accurate discrete Fourier transform to analyse the absolute phase of THz pulses

James Lloyd-Hughes\* and Nishtha Chopra

Department of Physics, University of Warwick, Gibbet Hill Road, Coventry, CV4 7AL, United Kingdom.

(Dated: September 4, 2024)

Electro-optic sampling allows the electric field of THz, mid-infrared and visible light pulses to be measured directly as a function of time, with data analysis often performed in the frequency domain after fast Fourier transform. Here we introduce a version of the discrete Fourier transform that is consistent with the analytical continuous Fourier transform, enabling the quantitative study of the amplitude and phase of light pulses without the phase ambiguity inherent in the conventional definition of the discrete Fourier transform. We then show that a phenomenological time-domain model, based on carrier and envelope waves, that can reproduce the wide variety of narrow-band and broadband multi- to single-cycle THz pulses reported in the literature, such as from spintronic emitters, photoconductive antennae, optical rectification and free electron lasers. We discuss the influence of the pulse envelope's duration, the carrier-envelope phase and the pulse arrival time on the complex spectra. The methodology and results described provide a valuable toolkit that unlocks the full potential of the phase information available in time-domain spectroscopy.

## I. INTRODUCTION

In time-domain ultrafast spectroscopy the electric field of a pulse of electromagnetic radiation,  $E(t)$ , is sampled experimentally as a function of time, and then Fourier transformed to obtain the complex spectra  $\tilde{E}(\omega) = |\tilde{E}(\omega)|e^{i\phi(\omega)}$  at angular frequency  $\omega$ . The amplitude spectrum,  $|\tilde{E}(\omega)|$ , represents the frequency content, while the phase  $\phi(\omega) = \angle\tilde{E}(\omega)$  marks the arrival time of each frequency component relative to zero time, where  $\angle$  denotes calculating the angle of the complex number. The well-established technique of terahertz time-domain spectroscopy (THz-TDS) makes full use of electro-optic sampling or photoconductive detection to record  $E(t)$  after interacting with a sample, where knowledge of the amplitude and phase gives the complex refractive index (complex dielectric function) of the material of interest [1]. While demonstrated first for THz pulses, time-domain spectroscopy has been widely utilised in the mid-infrared [2] and recently even in the visible (or “petahertz”) range [3, 4].

Although often only the amplitude spectrum is reported, the spectral phase,  $\phi(\omega)$ , contains a wealth of information about an electromagnetic pulse, including the pulse's arrival time (from the group delay) and the carrier-envelope phase of the pulse, which creates a frequency-independent offset to the spectral phase [5]. Further, the phase provides information about dispersive processes that occur during pulse generation, propagation, or detection. Propagation through a conductive or absorptive material can alter the spectral phase of a pulse, via its frequency-dependent refractive index [1]. Changes can even occur during propagation in free space: broadband electromagnetic pulses change spectral phase as a result of the geometric aberrations of the optical system, which alter the path length [6]; the Gouy effect causes the carrier-envelope phase to evolve as a beam propagates through a focus [7]. Schemes that modify the carrier-envelope phase of a THz pulse have been reported [5, 8], and are particularly important when using intense THz electric fields to drive non-linear processes, such as in THz scanning tunneling microscopy [8, 9].

In the vast majority of spectroscopy studies, rather than analysing complex spectra  $\tilde{E}(\omega)$ , analysis is instead performed on ratios of two different spectra,  $\tilde{E}_1(\omega)$  and  $\tilde{E}_2(\omega)$ . Such ratios are assumed to cancel out (to a first approximation) any changes in spectral phase as a result of propagation in the spectrometer or the detection process. For example, in transmission spectroscopy the complex transmission  $\tilde{T}(\omega) = \tilde{E}_2/\tilde{E}_1$  for sample spectrum  $\tilde{E}_2$  and reference spectrum  $\tilde{E}_1$  is analysed, including calculating the phase difference between  $\tilde{E}_1$  and  $\tilde{E}_2$ ,  $\Delta\phi(\omega) = \phi_2 - \phi_1$ . This *relative* phase provides information about differences in the optical path length, for example as a result of the introduction of a sample into the THz beam [1]. However, the *absolute* phases  $\phi_1(\omega)$  and  $\phi_2(\omega)$  are rarely reported.

Challenges associated with the accurate retrieval of the relative phase  $\Delta\phi(\omega)$  in THz-TDS have been discussed previously. In the context of transmission THz-TDS, Jepsen discussed difficulties in unwrapping the relative phase of sample and reference spectra, and provided an algorithm that made relative phase retrieval more robust by subtracting a linear phase term from sample and reference spectra [10]. In the reflection geometry, the extra path length that arises when samples are not placed at exactly the same location along the beam direction leads to a phase “error”, which can be corrected either experimentally by accurately positioning the reference mirror, or computationally [11].

---

\* j.lloyd-hughes@warwick.ac.uk

While these works identified how to improve analysis of the relative phase, they did not provide a way to reliably recover and utilise the absolute phase of the electromagnetic pulse.

In this Article we explore the absolute phase of electromagnetic pulses, using exemplary time-domain waveforms and complex spectra from THz-TDS. We show that the standard definition of the discrete Fourier transform, used in popular numerical libraries, does not accurately calculate the absolute phase spectrum. Herein, absolute phase refers to the phase calculated with respect to the centre of the electromagnetic pulse, and which is independent of the experimental sampling parameters. We provide a definition of the discrete Fourier transform that correctly determines the amplitude and absolute phase spectra, and verify it by comparison with analytical results from continuous Fourier transform (CFT) theory. We then construct a simple mathematical picture of free-space electromagnetic pulses in the time-domain that allows single- or multi-cycle waveforms to be fit to experimental data, either in the time-domain or the frequency-domain, for arbitrary carrier-envelope phases and pulse arrival times. Our accurate Fourier theory approach further allows us to:

- determine a unique arrival time for a pulse. For a few- or single-cycle pulse, as common in THz-TDS, this can be at the central zero of the electric field, rather than the peak electric field;
- examine the absolute phase of experimental waveforms, for example finding the carrier-envelope phase and the chirp created during electro-optic sampling;
- identify that the broadband THz pulses from an oscillator-driven photoconductive emitter have a sech envelope, rather than a Gaussian (as sometimes assumed).

The article is structured as follows. Section II explains why the standard discrete Fourier transform does not correctly return the absolute phase, and provides an accurate DFT that produces the same amplitude and phase spectra for simple waveforms as found analytically from the continuous Fourier transform. Section III then describes the application of Fourier theory to construct a model of electromagnetic pulses, including a discussion of the carrier-envelope phase and the pulse arrival time (group delay), valid for narrowband (multi-cycle) or broadband (single-cycle) pulses. The analysis of experimental data from THz-TDS in Section IV illustrates how these Fourier theory results can be used in practise. To avoid impeding the flow of the main text appendices provide useful results from Fourier theory, a python implementation of the DFT, and a description of how to deconvolve the electro-optic response function. The numerical routines we developed here are available online [12].

## II. AN AMPLITUDE- AND PHASE-ACCURATE DFT

The CFT can be used to calculate the spectrum of a real, continuous function  $E(t)$ , and is defined as  $\tilde{E}(\omega) = \int_{-\infty}^{\infty} E(t)e^{i\omega t} dt$ . In experiments, however,  $E(t)$  has to be sampled discretely, yielding a sequence  $E_m$ , where  $m = 0, 1, 2, \dots, n-1$  for  $n$  sampling points. The  $m$ th sample is at time  $t_m = m\delta t$ , while the width of the whole time window is  $T = n\delta t$ . As  $E_m$  is a discrete series, the discrete Fourier transform (DFT) has to be used to obtain the spectrum, defined by  $\tilde{E}_k = \sum_{m=0}^{n-1} E_m e^{i\omega_k t_m}$ , where the complex spectral component  $\tilde{E}_k$  is sampled at each angular frequency  $\omega_k = 2\pi k/(n\delta t)$  for  $k = 0, 1, 2, \dots, n-1$ . Note that if the experimental samples are not evenly spaced in time, then the data must first be interpolated onto a time axis with uniform spacing. Further, there are two definitions of the Fourier transform with either  $\pm i\omega t$ : here we adopted  $+i\omega t$  for the forwards DFT, while the opposite sign convention is adopted in some numerical packages. [13]

For functions  $E(t)$  where the CFT can be found analytically, the DFT calculated by computer should agree with the analytical CFT result. We now use this reasoning to derive a phase- and amplitude-accurate DFT.

### A. Derivation

By comparing the definitions of the CFT and the DFT we can see that in order for their amplitude spectra to match we require  $|\tilde{E}_k| \simeq |\tilde{E}(\omega = \omega_k)|$ , and hence the DFT definition, as normally stated, is missing the term  $\delta t$ . We therefore re-define the DFT as

$$\tilde{E}_k = \delta t \sum_{m=0}^{n-1} E_m e^{i\omega_k t_m} \quad (1)$$

in order to be consistent with the CFT. Parseval's theorem (Appendix A, Eqn. A4) can also be employed to check that the frequency-domain amplitude is correctly scaled, by ensuring that the time-domain and frequency-domain integrals match.

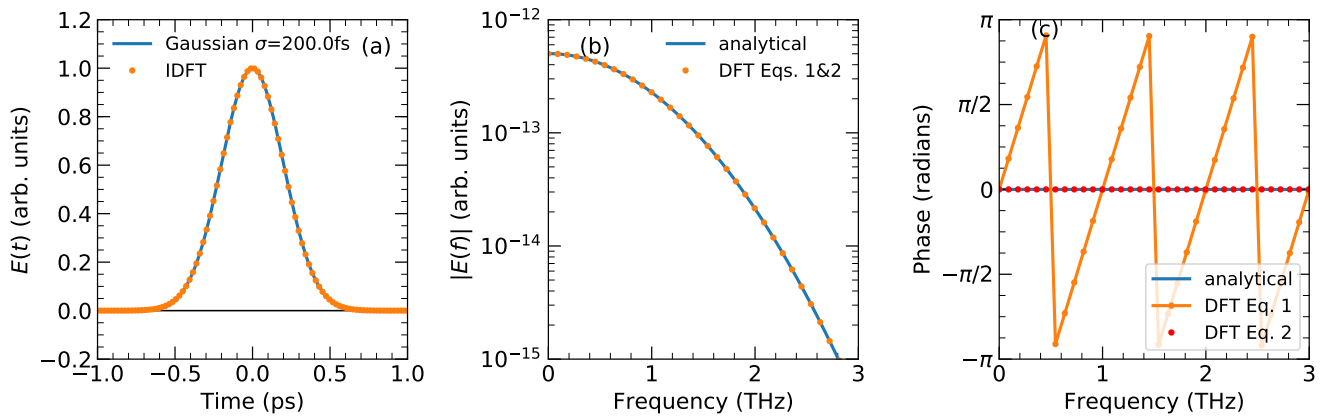


FIG. 1. (a) A Gaussian time-domain pulse (solid line), with  $\sigma = 200$  fs, sampled from  $t = -1$  ps, *i.e.* centred at a time  $t_0 = 1$  ps after the first point in the discrete time series. Points show the inverse DFT calculated from the spectra using Eqn. 5. (b) The amplitude spectra of (a) calculated from the CFT (solid line) and DFT from Eq. 1 and Eq. 2 (points). (c) The phase spectra from the CFT (blue line, at zero phase), the uncorrected DFT (Eq. 1, orange) and phase-corrected DFT (Eq. 2, red points). The uncorrected DFT has a linear slope with gradient  $2\pi t_0$ , whereas the phase-corrected DFT reproduces the zero phase expected analytically.

Although the mathematical form of the DFT and CFT now look similar, there is an additional subtlety hidden in requiring that the phase returned by the DFT should match that of the CFT, or  $\angle \tilde{E}_k = \angle \tilde{E}(\omega = \omega_k)$ . This requirement is not ensured by Equation 1, which is “blind” to the absolute time  $t$ . The DFT as stated above (and in standard numerical libraries [13]) considers the time  $t_m = m\delta t$  relative to the first time point sampled in the series, at  $m = 0$ . Hence the phase  $\phi_k = \angle \tilde{E}_k$  using Equation 1 is determined relative to that of the first time point in the series, rather than reporting the absolute phase  $\phi(\omega = \omega_k)$ . In experiments measuring a pulse this definition is therefore unsatisfactory, as the relative phase  $\phi_k$  returned from the standard DFT varies with the length of the sampling window before the pulse. To determine the absolute phase correctly, we propose the following definition of the DFT:

$$\tilde{E}(\omega_k) = \delta t \sum_{m=0}^{n-1} E_m e^{i\omega_k(t_m - t_0)} = \delta t \cdot e^{-i\omega_k t_0} \sum_{m=0}^{n-1} E_m e^{i\omega_k t_m} \quad (2)$$

where the term  $e^{-i\omega_k t_0}$  accounts for the finite arrival time of the pulse at element  $m_0$  and time  $t_0 = m_0 \delta t$  after the first time point, and the factor  $\delta t$  gives the correct amplitude. Note that throughout we adopt  $\tilde{E}(\omega_k)$  to refer to the phase- and amplitude-correct DFT of Equation 2, and use  $\tilde{E}_k$  to denote the DFT of Equation 1, which has the correct amplitude but the wrong phase.

This phase-corrected DFT equation is derived below, but is first validated by comparison to the spectrum of a Gaussian input pulse calculated from the analytical CFT. A Gaussian input pulse, centred at zero time and with the form  $g(t) = A e^{-t^2/2\sigma^2}$ , is pictured in Fig. 1(a) for  $A = 1$  and  $\sigma = 200$  fs. The amplitude and phase of  $\tilde{g}(\omega)$  from the CFT are shown in Fig. 1(b) and (c) [solid blue lines]. Since  $g(t)$  is a real, even function, the CFT  $\tilde{g}(\omega) = \int_{-\infty}^{\infty} g(t) e^{i\omega t} dt = \sqrt{2\pi\sigma^2} e^{-\omega^2\sigma^2/2}$  is purely real, and therefore has zero argument, *i.e.* zero phase. While the amplitude-corrected DFT (Equation 1) applied to the same, discretely sampled Gaussian function  $g_m$  yields the correct amplitude spectrum (points in panel (b)) it returns the wrong phase (orange points in panel (c)). Rather than zero, the phase is a straight line, and phase jumps of  $-2\pi$  occur every time the phase increases above  $\pi$  (these can be straightforwardly unwrapped if needed). In contrast, Equation 2 returns the same amplitude (orange points in (b)) and also phase (red points in (c)) as the CFT, demonstrating that the new definition of the DFT in Equation 2 accurately reproduces the correct absolute phase in this case.

Note that the incorrect linear phase returned from the standard DFT expression (Equation 1) should not be misinterpreted as arising from anything physical: for example in THz-TDS one’s physical intuition might be tempted to link this linear phase to light propagation through a finite distance  $L$ , since the phase of the electric field in that case is  $\phi(\omega) = \omega L/c$ . Rather, the linear phase returned by the standard DFT is a result of the discrete series peaking at time  $t_0 = m_0 \delta t$  from the first element ( $t_0 = 1$  ps in this case). Changing the sampling window to start earlier or later in time alters the phase calculated from Equation 1. Thus Equation 1 does not reproduce the expected zero phase

of the CFT, nor does the linear phase represent anything physical (there should be no difference in  $\tilde{E}(\omega)$  for data sampled with different time windows). Further, having a large linear phase can lead to significant phase unwrapping problems when the gradient is particularly high, such that phase jumps of  $2\pi$  can occur within one step in frequency, as described in detail in Ref. 10.

To derive the phase-corrected DFT of Eqn. 2 we return to the example of the discretely sampled Gaussian. This peaks at element  $m_0$  (time  $t_0$ ), and hence has the form  $g_m = Ae^{-(t_m - t_0)^2}/2\sigma^2$ . Using Equation 1 the DFT of the discretely-sampled Gaussian,  $\tilde{g}_k$ , therefore approximates the continuous Fourier transform of the time-shifted continuous function  $g(t - t_0)$ , or:

$$\tilde{g}_k \simeq \mathcal{F}[g(t - t_0)] = e^{i\omega t_0} \tilde{g}(\omega) \quad (3)$$

where  $\tilde{g}(\omega)$  is as above, and the second equality is via the Fourier time-shift theorem. The CFT of the time-shifted pulse, and the DFT of the Gaussian series, therefore both have a finite argument,  $\omega t_0$ , rather than the zero phase expected for the CFT of a Gaussian centred at  $t = 0$ . Re-arranging Equation 3, one finds that the desired information, the complex spectrum  $\tilde{g}(\omega)$  of a Gaussian, can be obtained from  $\tilde{g}(\omega) \simeq e^{-i\omega t_0} \tilde{g}_k$ .

While this specific example discussed the FT of a Gaussian, the Fourier shift theorem applies generally to an arbitrary input pulse  $E(t)$ , and hence we generalise to write  $\tilde{E}(\omega_k) = e^{-i\omega_k t_0} \mathcal{F}[E(t - t_0)] \simeq e^{-i\omega_k t_0} \tilde{E}_k$ . This result allows one to derive the phase-corrected DFT of Equation 2 from the phase-ambiguous version in Equation 1.

An example of how to implement the amplitude- and phase-corrected DFT is provided in the Python code presented in Appendix B.

## B. Inverse transform

Similar considerations allow us to define a corrected inverse DFT that can convert a complex, frequency-domain signal into the time-domain. The inverse CFT is:

$$E(t) = \frac{1}{2\pi} \int_{-\infty}^{\infty} \tilde{E}(\omega) e^{-i\omega t} d\omega, \quad (4)$$

and the amplitude- and phase-corrected inverse DFT has the form

$$E_m = \frac{1}{n\delta t} \sum_{k=0}^{n-1} \tilde{E}_k e^{-i\omega_k t_m} \quad (5)$$

where  $\tilde{E}_k = \tilde{E}(\omega_k) e^{i\omega_k t_0}$ . The scaling factor  $1/(n\delta t)$  ensures the correct amplitude, and can be derived by considering that  $\delta\omega = \omega_{k+1} - \omega_k = 2\pi/(n\delta t)$ . The validity of the phase-corrected inverse DFT is demonstrated in Fig. 1(a), where the points show  $E_m$  obtained from Eqn. 5 applied to the complex spectrum of the Gaussian.

## III. A SIMPLE MODEL OF A THZ PULSE

The electromagnetic pulses from common laser-based THz sources, such as photoconductive switches [14, 15], optical rectification [16, 17], and spintronic emitters [18] are often close to single-cycle in shape. Multi-cycle THz pulses can be obtained from optical rectification [19], photoconductive antenna arrays [20, 21], quantum cascade lasers [22], or free electron lasers [23]. In this Section we establish simple expressions for the time- and frequency-domain waveforms of single- and few-cycle electromagnetic pulses. This provides a straightforward parameterisation of a THz pulse that can model single- or multi-cycle THz pulses. The frequency-domain analytical results were verified by comparison to the phase-accurate DFT of the time-domain model. By first discussing the analytical model in this section, with insights from our amplitude- and phase-correct Fourier theory, we provide a pedagogical treatment of the expected amplitude and phase spectra of typical pulsed THz sources, before providing a comparison with experiment in Section IV.

### A. Carrier-envelope model

To provide a phenomenological time-domain model of a few-cycle THz pulse we consider the electric field to be the product of a carrier wave, described by the function  $f_c(t)$ , and an envelope function  $f_e(t)$ , *i.e.*  $E(t) = f_c(t)f_e(t)$ . Note

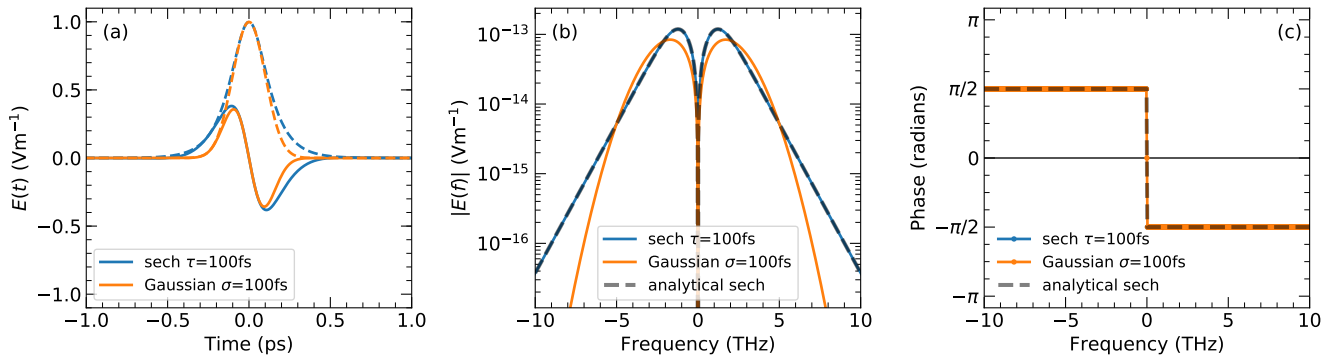


FIG. 2. THz pulses calculated for sech (blue lines) or gaussian (orange lines) pulse envelopes. (a) Indicates the time-domain waveforms (solid lines) for a sech envelope (blue dashed line) or gaussian envelope (orange dashed line). A 1 THz carrier frequency was assumed, with zero carrier and envelope offset times, and  $\tau = \sigma = 100$  fs. (b) Amplitude spectra from the DFT of the THz pulses in (a), along with the analytical result for the CFT of a sech pulse (dashed line). (c) Phase spectra of data in (a) from DFT and CFT.

that the following is not an attempt to model the pulse shape of THz radiation based on the physics of the generation mechanism in the source, nor does it consider the impact of the propagation of THz radiation through a material or an optical system. Rather, the goal in this section is to derive a simple, phenomenological picture of THz pulses in the time-domain and, via the corrected discrete Fourier transform or analytical CFT, in the frequency domain.

For the carrier wave we assumed  $f_c(t) = -\sin(\omega_c(t - t_{\text{CEP}}))$ , where  $t_{\text{CEP}} = t_c - t_e$  is the carrier-envelope phase difference, namely the time difference between the zero time of the envelope function,  $t_e$ , and carrier wave,  $t_c$ . The minus sign in front of the carrier wave ensures by convention that the first half-cycle is positive for small  $t_{\text{CEP}}$ . We consider two possibilities for the envelope function, which is centred at  $t_e$ , close to zero delay ( $t = 0$ ): a Gaussian envelope,  $f_e(t) = Ae^{-(t-t_e)^2/2\sigma^2}$ , or a sech envelope,  $f_e(t) = A\text{sech}((t - t_e)/\tau)$ . This yields, for the sech case:

$$E(t) = -A\text{sech}((t - t_e)/\tau) \sin(\omega_c(t - t_{\text{CEP}})). \quad (6)$$

As discussed in Ref. [24], the carrier-envelope model does not produce realistic electric field pulses for short pulse envelopes ( $\tau \leq 2\pi/\omega_c$ ) if the carrier-envelope phase is such that the carrier wave becomes close to a cosine (e.g. when  $\omega_c t_{\text{CEP}} = \pi/2$ ). In this case the spectral amplitude is non-zero at zero frequency, which is not physical for electromagnetic pulses in the far-field (where the electric field depends on a time derivative, hence has no dc component) [24]. Here, the choice of a sine carrier wave allows pulses that are close to single-cycle to be modelled when the carrier-envelope phase offset  $\omega_c t_{\text{CEP}}$  is close to zero or  $\pi$ , as the spectral amplitude drops to zero at zero frequency. This approach is valid when  $t_c = t_e$ , i.e. zero carrier-envelope phase, which we consider in this section, while a version of the model valid for all CEPs is presented in Sec. III C.

In Figure 2(a) THz pulses  $E(t)$  are shown with  $A = 1\text{Vm}^{-1}$  for the two envelope functions, with  $\tau = \sigma = 100$  fs and  $t_e = t_c = t_{\text{CEP}} = 0$ . The THz pulse with the sech envelope (solid blue line) has broader wings in time than the THz pulse with the Gaussian envelope (solid orange line). This is a result of the exponential time-dependence at large times of the sech pulse envelope (blue, dashed), which drops slower than a Gaussian envelope (orange, dashed). In the frequency domain, the DFT of the THz pulses with sech and gaussian envelopes are reported in Fig. 2(b) and (c), as calculated using equation 2. The DFT of the sech pulse exhibits an amplitude spectrum (panel b, blue line) that decreases exponentially at high frequencies. In contrast,  $|E(\omega)|$  for the Gaussian envelope has a Gaussian spectral shape, and hence decreases more rapidly at high frequencies than the sech pulse. Thus, despite the apparently longer time-domain envelope for the sech envelope, at higher frequencies (above 5 THz for this particular case) sech pulses have larger spectral amplitude than Gaussian pulses.

The CFT of the model THz pulse  $E(t) = f_c(t)f_e(t)$ , valid for zero carrier-envelope phase, can be derived analytically using the standard Fourier theory expressions provided in Appendix A. For example, for a sech pulse envelope with  $t_e = t_c = 0$ , using Equations A3 and A7 yields:

$$\tilde{E}(\omega) = iA \frac{\pi\tau}{2} \left[ \text{sech} \left( \frac{\pi\tau}{2} (\omega + \omega_c) \right) - \text{sech} \left( \frac{\pi\tau}{2} (\omega - \omega_c) \right) \right] \quad (7)$$

where the THz pulse has a purely imaginary spectrum as a result of the time-domain being an odd function. The CFT result, shown by the dashed lines in Fig. 2(b) and (c), is in excellent agreement with the DFT calculation from

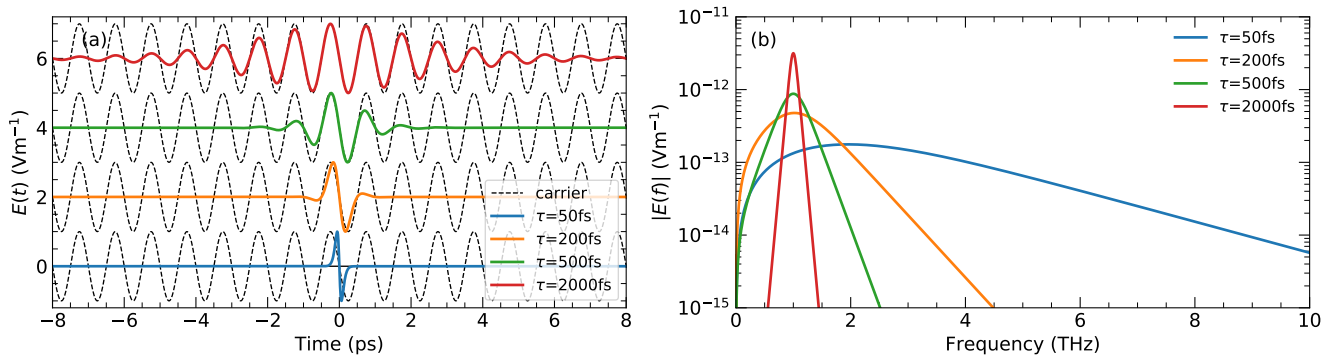


FIG. 3. (a). Time-domain THz pulses for a sech envelope with different pulse durations,  $\tau = 50$  fs to 2000 fs (coloured lines). Waveforms are offset for clarity. Dashed lines indicate the carrier wave (1 THz frequency, or 1 ps period). (b) Amplitude spectra of the THz pulses in (a).

Equation 2. The phase (Fig. 2c) is  $\pm\pi/2$ , as the spectrum in Eqn. 7 is purely imaginary ( $e^{\pm i\pi/2} = \pm i$ ). Further, the phase undergoes a  $\pi$  change across zero frequency as a result of the two  $\delta$ -functions in Equation A1 having opposite sign.

It is worth noting that both positive and negative frequencies are plotted in Fig. 2(b) and (c) in order to show the behaviour across  $\omega = 0$ . A mathematical justification for the need to include negative frequency components is that the CFT of a sine wave contains delta functions centred at both negative and positive frequencies.

### B. Influence of pulse duration: spectral slope

To demonstrate the impact of the envelope pulse's duration on the time- and frequency-domain, we report in Figure 3 results calculated using Equations 6 and 7 for a sech envelope with various values of  $\tau$ . The time-domain waveforms were normalised to have amplitude  $1 \text{ Vm}^{-1}$ . When  $\tau$  was larger, the multi-cycle THz pulse (red line in panel (a),  $\tau = 2$  ps) tracked the oscillations of the carrier wave (dashed line), while the Fourier amplitude spectrum was relatively narrow and was centred at the carrier wave frequency (1 THz). This waveform is representative of narrow-band THz pulses containing a few cycles, such as produced by some optical rectification schemes [19], while mode-locked THz QCLs [22] and THz FELs [23] generate multi-cycle THz pulses with even larger pulse envelopes.

When the envelope pulse duration was lowered to  $\tau = 200$  fs or 500 fs, the waveform and spectra (yellow and green lines in Fig. 3) became more representative of broadband THz generation, such as achieved via typical optical rectification using laser amplifiers (e.g. in  $\text{LiNbO}_3$  via the tilted-pulse method, or using ZnTe or GaP). For pulse durations below  $\tau = 100$  fs, the spectrum became ultra-broadband: the spectral peak shifted to higher frequencies, and the gradient of the amplitude spectrum at high frequencies – the *spectral slope* – became more shallow. Noting that for a sech envelope the gradient of the amplitude spectrum on a logarithmic  $y$ -axis is linear at high frequencies  $\omega \gg \omega_c$  (Figure 3(b) and Figure 2(b)), we derive an expression for the spectral slope. In this limit, the amplitude spectrum can be calculated from Equation 7:

$$|\tilde{E}(\omega \rightarrow \infty)| \approx |A| \frac{\pi\tau}{2} \operatorname{sech}\left(\frac{\pi\tau}{2}\omega\right) = |A| \frac{\pi\tau}{2} \frac{2}{e^{\pi\tau\omega/2} + e^{-\pi\tau\omega/2}} \approx |A| \pi\tau e^{-\pi\tau\omega/2}. \quad (8)$$

From this equation, we can deduce that the amplitude spectrum drops exponentially at high frequencies for a sech pulse envelope, and hence has a negative straight line when plotted with a log  $y$ -axis (e.g. Figure 3 (b)). Since  $\ln|\tilde{E}(\omega \rightarrow \infty)| = \ln|A|\pi\tau - \pi\tau\omega/2$ , the gradient is  $d|\tilde{E}(\omega \rightarrow \infty)|/d\omega = -\pi\tau/2$ . This depends only on the duration of the pulse envelope. Hence a linear spectral slope (with a logarithmic  $y$ -axis) implies a sech time-domain envelope, and yields the pulse duration  $\tau$ .

### C. Influence of pulse arrival and phase offset

The influence of the pulse arrival time and carrier-envelope phase is reported in Fig. 4. In panels (a) and (b), single-cycle THz pulses are shown arriving at different times  $t_e$  from -200 fs to 200 fs, and keeping  $t_{\text{CEP}} = 0$  to first

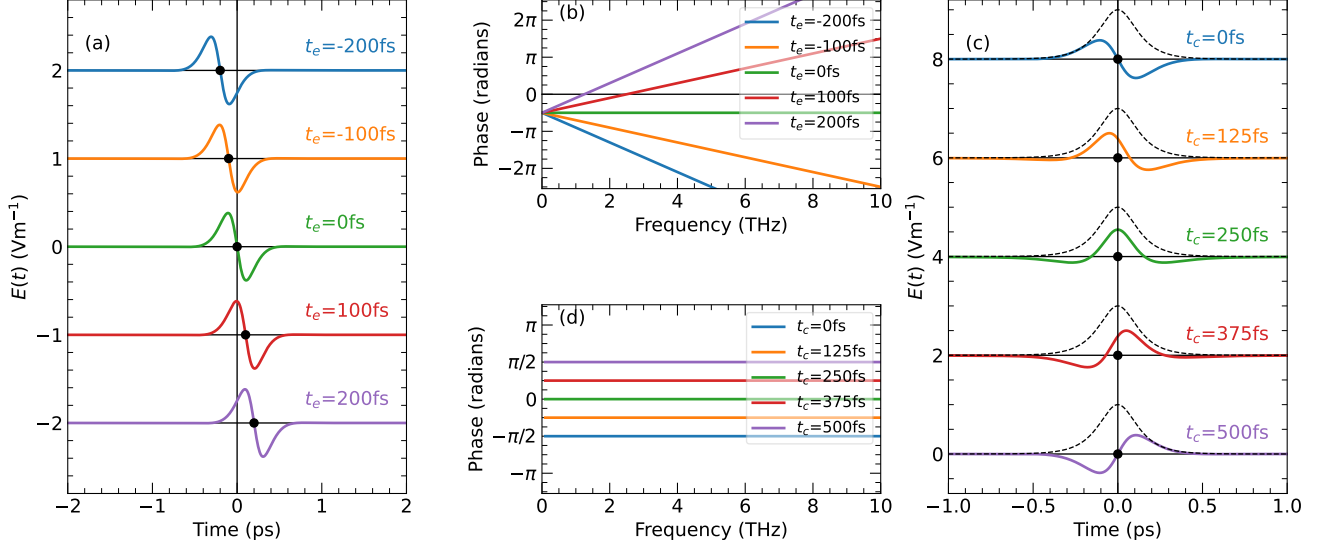


FIG. 4. (a) THz time-domain pulses calculated using Eqn. 6 with  $\omega/2\pi = 1$  THz,  $\tau = 100$  fs,  $t_{\text{CEP}} = 0$  and various values of  $t_e$ . Black points indicate the pulse arrival time (mean arrival time method). Pulses are plotted offset vertically for clarity. (b) Unwrapped phase spectra from DFT of data in (a). (c) THz pulses with  $t_e = 0$ , and varying carrier times  $0 \leq t_c \leq 500$  fs, corresponding to different carrier-envelope phases  $0 \leq \phi \leq \pi$ . The dashed lines indicate the sech envelope, and the black points are the mean arrival time. (d) Phase spectra corresponding to the cases shown in (c).

discuss the case with zero carrier-envelope phase. The amplitude spectra (not shown) are identical, but by the Fourier shift theorem changing the centre times of the THz pulse envelope (black dots in panel (a)) produces a linear gradient to the phase, shown unwrapped in panel (b). The case with  $t_e = 0$  produces a constant absolute phase  $-\pi/2$ .

In order to produce physically realistic broadband time-domain pulses even in the case of finite carrier-envelope phase (as discussed above with reference to Ref. [24]) we follow Ahmed *et al.*'s procedure and take the DFT of Eqn. 6 with  $t_{\text{CEP}} = 0$ , multiplying the complex spectrum by the Heaviside step function,  $\Theta(\omega)$ , and taking the inverse DFT. This produces an analytic representation of the electric field,  $\tilde{E}(t)$ , a complex time-domain function with no negative frequency components. The physical electric field after a phase shift can then be determined from:

$$E(t) = \Re(2e^{i\phi}\tilde{E}(t)) = \Re\left(2e^{i\phi}\mathcal{F}^{-1}\left[\Theta(\omega)\tilde{E}(\omega)\right]\right), \quad (9)$$

where  $\phi = \omega_c t_{\text{CEP}}$  is the carrier-envelope phase shift. The factor of 2 corrects the complex representation to have the same amplitude as the original electric field (since half of the amplitude is discarded by the Heaviside function).

Representative THz pulses for different carrier-envelope phases are reported in Fig. 4(c)-(d), obtained by setting  $t_e = 0$  and varying  $t_c$ . As  $t_c$  increased, the waveform changed shape from single-cycle ( $t_c = 0$ ) to become closer to a symmetric half cycle ( $t_c = 250$  fs), as the carrier wave became more like a cosine. A THz pulse with a symmetric shape about the pulse centre ( $\omega_c t_c = \pm\pi/2$ ) is an even function ( $E(-t) = E(t)$ ), and hence via Fourier theory has a purely real Fourier spectrum with zero phase, as can be seen in panel (d). Conversely,  $\omega_c t_c = \{0, \pi\}$  results in an odd function ( $E(-t) = -E(t)$ ) and a purely imaginary spectrum with  $\phi(\omega) = \pm\pi/2$ . These cases can be seen in panel (d), where  $t_c = 250$  fs corresponds to  $\omega_c t_c = \pi/2$ , and  $t_c = 500$  fs corresponds to  $\omega_c t_c = \pi$ .

#### D. Pulse arrival time

The definition of the phase-accurate DFT in Sec. II implicitly assumes that the time,  $t_0$ , from the first point in the series to the centre of the pulse, is known. While this is the case if the waveform is calculated from an analytical expression (*e.g.* Eqn. 6), for an experimental waveform the value of  $t_0$  needs to be input or determined by the DFT routine. Here we provide various approaches to determining the pulse arrival time:

1. **Educated guess.** If the THz pulse is close to single-cycle in shape, manually read the time delay where the electric field changes sign between the positive and negative extrema. If the THz pulse is more like a symmetric half-cycle, take the time delay of the largest peak.

2. **Mean arrival time.** Calculate the mean arrival time of the pulse, based on the first-order moment of the normalised intensity,  $\langle t \rangle = \int_{-\infty}^{\infty} tI(t)dt$ , where  $I(t) = E^2(t)/\int_{-\infty}^{\infty} E^2(t)dt$ .
3. **Time-domain fit.** Fit an analytical model of the electric field, such as Eqn. 6, to determine the arrival time of the envelope.
4. **Group delay.** The first derivative of the spectral phase  $\phi(\omega)$  is called the group delay,  $t_g(\omega) = d\phi/d\omega$ . Evaluating the group delay at the frequency of maximum spectral amplitude,  $\omega_m$ , allows the arrival time of the pulse to be determined. This result can be understood from the Fourier shift theorem, as the linear component of the spectral phase corresponds to a delay in the time domain.

The solid circles in Fig. 4(a) and (c) indicate the pulse arrival times calculated using the mean arrival time method, and agree exactly with the input envelope times, indicating that the method works in this case. However the accuracy of the methods does depend on the complexity of the spectral phase. The “educated guess” method requires no extra calculations but requires the experimenter’s input, and is thus not automated or as precise as the other methods. With finite carrier-envelope phase (e.g.  $t_c = 125$  fs in Fig. 4(c)), the educated guess method predicts the wrong arrival time, since the zero crossing is not at the peak of the pulse envelope. The mean arrival time can be calculated rapidly via numerical integration, and is accurate for pulses that are not too complex. However it cannot be used for more complex waveforms: for instance if the data set comprises a pulse train created by internal reflections, the time returned by the integral will be pulled later in time by the pulse echoes. The time-domain fit method is more complex to implement, but can be extended to cope with situations involving multiple pulses. Finally, the group-delay method is simpler than the time-domain fit to implement, and yields the same results as the mean arrival time method if the pulse is relatively simple (i.e. if the spectral phase is relatively flat). However the group-delay method stumbles if the spectral phase has a complex shape at the frequency of the maximum spectral amplitude. This can be the case, for example, if the THz pulse has undergone strong dispersion as a result of a resonance near the maximum frequency, or from multiple internal reflections [25].

## IV. EXPERIMENTAL RESULTS

Armed with the insights presented in the previous sections, we now discuss literature reports of the experimental phase spectra obtained using electro-optic sampling, as well as providing an analysis of our own experimental results.

### A. Literature reports of spectral phase

Only a limited number of papers in the time-domain spectroscopy community have reported the spectral phase, of which the following is a representative (but non-exhaustive!) list. Leitenstorfer *et al.* [26] reported ultrabroadband amplitude and phase spectra from  $p-i-n$  diodes, with complex phase that decreased from 3 rad at low frequency to 1 rad at 3 THz, before remaining relatively flat up to the LO-phonon frequency of InP, where it varied rapidly. Kübler *et al.* showed the electric field of ultrabroadband mid-infrared pulses produced and detected by GaSe, with a spectral maximum at 30 THz [27]. They assumed a Gaussian envelope for the 3-cycle electric field pulse, which had 28 fs duration. The spectral phase was below 1 rad from 10 THz to 100 THz, which is consistent with their cosine-like electro-optic signal and our discussion above with reference to Fig. 4. Knorr *et al.* reported the electric field of 20 THz mid-infrared pulses detected using thin GaSe flakes [25], and showed a relatively flat spectral phase from 15 THz to 30 THz, but which rapidly increased at lower frequencies. The carrier-envelope phase was not determined, as the time-domain peak electric field was assumed to be the centre of the pulse envelope. Ultrabroadband THz pulses from spintronic emitters were first reported by Seifert *et al.* [18], and were found to have close to zero spectral phase over a 30 THz bandwidth, signifying chirp-free (Fourier limited) pulse durations. However, this cannot be seen straightforwardly from the reported time-domain electro-optic signal, which had a finite pulse arrival time (250 fs), which would imply a linear slope to the phase (not reported), and an asymmetric pulse shape, which should give finite (non-zero) CEP (Fig. 4).

In the above experimental works the spectral phase was not used to uncover the carrier-envelope phase or the group delay. An extension of frequency-resolved optical grating (FROG) was reported to yield the CEP of a half-cycle THz pulse [28] to be around  $2^\circ$ . While the electric-field waveform from the retrieved FROG spectrogram was similar to that directly obtained from EOS, the spectral phase from EOS was not reported. Control of the CEP for a THz pulse was reported using Fresnel prisms [5], where the input pulses had a complicated  $\phi(\omega)$  ranging from  $\phi(0.5\text{THz}) = -1.5$  rad, to  $\phi(1.75\text{THz}) = 0$  rad, to  $\phi(2.5\text{THz}) = -2.5$  rad. Although the origin of this complex  $\phi(\omega)$  was not discussed, and the absolute spectral phase was not used to determine the CEP, rotating the Fresnel prisms did produce the expected



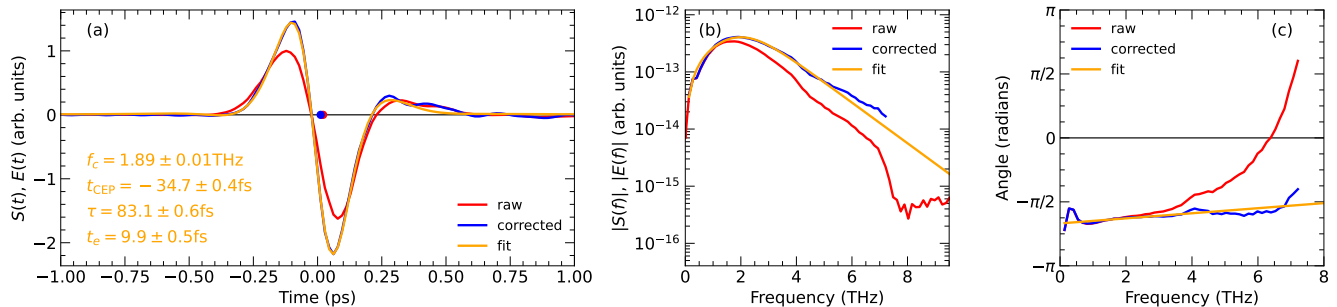


FIG. 5. Experimental THz pulse emitted by a photoconductive emitter, compared with the THz pulse model. (a) Raw electro-optic signal  $S(t)$  before deconvolving the detector's response (red); after deconvolving the detector's response (blue). A fit using Equation 6 is shown by the orange line. (b) and (c) show the amplitude and phase DFT spectra of the data in (a).

changes in CEP (using the difference in spectral phase for different prism angles). Allerbeck *et al.* demonstrated how to modify the CEP of a THz pulse using frustrated total internal reflection in a prism coupled to a metal mirror [8]. A carrier-envelope phase model (similar to Eqn. 6 but with a Gaussian envelope), and which is not fully valid for single-cycle pulses with arbitrary CEP [24], was used to fit the time-domain waveforms and infer the CEP [8]. Finally, Zhang *et al.* examined the spectral phase of the THz radiation produced by a DC-biased laser-induced plasma in air, and found that changing the position of the bias along the filament altered the CEP of the THz pulse, as deduced from the zero-frequency limit of the spectral phase [29].

## B. Experimental phase spectra

Here we provide a detailed analysis of the spectral phase of a typical source of pulsed THz radiation, in order to demonstrate that the CEP, group delay and chirp can be readily obtained from the spectral phase. We recorded the time-domain THz waveform from an interdigitated photoconductive switch, made on semi-insulating GaAs and photoexcited with 800 nm central wavelength pulses from a mode-locked Ti:sapphire oscillator (Newport Spectra Physics Mai Tai) with a pulse duration of 100 fs [30]. Four off-axis parabolic mirrors (3" focal length, 2" diameter) were placed in a  $(a, a)(a, a)$  geometry, as described in Ref. [6], to collect and focus the THz radiation to the sample plane and then the detection crystal. Electro-optic sampling was performed using a 200  $\mu\text{m}$ -thick (111)-oriented GaP detection crystal on a 1 mm-thick (100) GaP substrate. The entire THz beam path was purged with nitrogen gas.

We report in Figure 5 the time- and frequency-domain electro-optic signals,  $S(t)$  and  $\tilde{S}(\omega)$ , obtained for this spectrometer (red curves). The pulse was close to single-cycle in shape [panel (a)], and had frequency components spanning from 100 GHz to 7.5 THz [panel (b)] before hitting the noise floor at  $7 \times 10^{-16}$ . The absolute phase of the electro-optic signal, reported in Fig. 5(c), started close to  $-\pi/2$  at low frequencies, as expected based on the discussion in Section III. While the spectral phase was relatively flat to 3.5 THz, at higher frequencies the phase began to increase dramatically. This can be understood as a result of the electro-optic sampling process: the measured electro-optic signal does not have exactly the same temporal shape as the true electric field of the THz pulse incident on the detection crystal [26, 31]. For example, in the crystal the phase velocity of THz radiation and the group velocity of the infrared gate pulse are different, and hence after propagating some distance through the crystal they may no longer be in phase. This introduces a non-linear spectral phase, or chirp, to the electro-optic signal. Deconvolving the detector's complex response function is well described in the literature [26, 31, 32], and we detail our particular implementation in Appendix C.

Correcting for the response function,  $\tilde{R}(\omega)$ , of the 200  $\mu\text{m}$ -thick GaP electro-optic crystal over the range below 7.5 THz produces the blue lines in panels (b) and (c), which show the amplitude and phase of the electric field. Above 7.5 THz the electro-optic signal could not be corrected, as the response function had a minimum strong enough that the electro-optic signal dropped below the noise floor. The spectral amplitude of the electric field is marginally higher than the electro-optic signal in the range 2 THz to 7.5 THz as a result of  $|\tilde{R}(\omega)|$  being less than 1 in this range. After correction, the spectral phase is much flatter, implying that the THz pulse incident onto the detector was relatively free of chirp.

The time-domain  $E(t)$  pulse was close to single-cycle in shape, and can be accurately modelled via Equation 9, as illustrated by the yellow line in Fig. 5(a). A time-domain fit yielded a pulse arrival time  $t_e = 9.9 \pm 0.4$  fs and duration  $\tau = 83 \pm 1$  fs, along with a carrier frequency  $f_c = 1.89 \pm 0.01$  THz and carrier-envelope time  $t_{\text{CEP}} = -35 \pm 1$  fs. The

amplitude and phase of the model in the frequency domain are also in good agreement with the experimental data. In particular, the small negative  $t_{\text{CEP}}$  reduced the constant spectral phase  $\phi(\omega \rightarrow 0)$  below  $-\pi/2$  (panel (c)), while the small  $t_e$  gave the spectral phase a small positive slope. It is also clear that the THz pulse envelope was as short as possible: it had minimal chirp, and a duration that was similar to the specified duration of the fs laser used (100 fs).

Finally, the shape of the experimental THz spectrum was consistent with a sech pulse envelope, rather than a Gaussian. In the frequency domain a Gaussian pulse's amplitude drops too rapidly compared to the experimental amplitude, whereas a sech envelope yields the observed exponential dependence. A sech pulse envelope is expected in the case that the THz pulse duration is limited by the temporal envelope of the fs laser, and sech pulse envelopes are typical of the fs laser oscillator used.

## V. CONCLUSION

In this Article we presented aspects of Fourier theory as applied to electromagnetic pulses, including a phase- and amplitude-accurate discrete Fourier transform, and a simple model of single- and multi-cycle light pulses. Our aim was to provide a single reference that provides insights into pulse analysis for time-domain ultrafast spectroscopy methods. Although we presented and validated our methods using data from THz time-domain spectroscopy, the approaches summarised here are equally applicable to mid-infrared and visible time-domain spectroscopic methods that use electro-optic sampling (or similar approaches) to uncover the electric field of light pulses. The time- or frequency-domain model provided, when fit to experimental data, provides useful insights into the properties of such pulses, namely the pulse arrival time (group delay), carrier-envelope phase, and inherent chirp of the pulse. The accurate determination of the pulse arrival time may prove useful in THz time-of-flight, layer thickness or tomography applications [33], while the ability to find the carrier-envelope phase more easily will allow setups to be optimised for maximal peak electric field [8]. The methods described may find use in other areas of ultrafast spectroscopy, such as multidimensional coherent spectroscopy [34], which use Fourier transforms to perform data analysis.

## ACKNOWLEDGMENTS

The authors would like to acknowledge funding from the EPSRC (UK) (Grant No. EP/V047914/1).

### Appendix A: Useful results from Fourier theory

#### 1. Continuous Fourier transforms

Some standard Fourier transforms that are of use to model ultrafast pulses of light are as follows.

*Sine.* The strongest frequency component of a light pulse is its ‘‘carrier frequency,’’ the frequency of the maximum spectral amplitude. For a time-domain sine wave  $f(t) = \sin(\omega_c t)$  oscillating with angular carrier frequency  $\omega_c$  the CFT is

$$\tilde{f}(\omega) = i\pi (\delta(\omega - \omega_c) - \delta(\omega + \omega_c)). \quad (\text{A1})$$

*Gaussian.* As a standard function, the Gaussian or normal distribution is often used to model the envelope of a light pulse. For a Gaussian profile centred at time  $t = 0$ , the pulse can be described by  $g(t) = Ae^{-t^2/2\sigma^2}$ , where a shorter pulse has smaller standard deviation  $\sigma$ . The CFT of  $g(t)$  is then

$$\tilde{g}(\omega) = \int_{-\infty}^{\infty} g(t)e^{i\omega t} dt = \sqrt{2\pi\sigma^2}e^{-\omega^2\sigma^2/2}, \quad (\text{A2})$$

and hence the Fourier transform of a Gaussian time-domain signal has a Gaussian profile in the frequency domain.

*sech.* The hyperbolic secant function,  $\text{sech}(t) = 1/\cosh(t) = 2/(e^t + e^{-t})$ , is often used to model the pulse envelope of light pulses from femtosecond lasers. Writing the pulse envelope as  $f_e(t) = \text{sech}(t/\tau)$  for pulse duration  $\tau$ , the CFT is

$$\tilde{f}_e(\omega) = \pi\tau \text{sech}\left(\frac{\pi\tau}{2}\omega\right), \quad (\text{A3})$$

and hence the Fourier transform of a sech time-domain signal also has a sech profile in the frequency domain.

## 2. Useful Fourier relationships

*Parseval's theorem.* The integral of the modulus squared of a function in the time-domain and frequency-domain are linked by Parseval's theorem:

$$\int_{-\infty}^{\infty} |E(t)|^2 dt = \frac{1}{2\pi} \int_{-\infty}^{\infty} |\tilde{E}(\omega)|^2 d\omega, \quad (\text{A4})$$

or in discrete form:

$$\sum_{m=-\infty}^{\infty} |E_m(t_m)|^2 \delta t = \frac{1}{2\pi} \sum_{k=-\infty}^{\infty} |\tilde{E}_k(\omega_k)|^2 \delta \omega_k. \quad (\text{A5})$$

for discrete times  $t_m$  and discrete angular frequencies  $\delta \omega_k$ . Parseval's theorem can be used to verify numerically whether the amplitude spectrum of the discrete Fourier transform is scaled correctly, by comparison to the sum (or integral) of the time-domain.

*Fourier shift theorem.* For a function  $f(t)$  with Fourier transform  $\tilde{f}(\omega)$ , if the function is shifted in the time-domain to  $f(t - t_0)$ , then the Fourier transform of the shifted function can be written

$$\mathcal{F}[f(t - t_0)] = e^{i\omega t_0} \tilde{f}(\omega). \quad (\text{A6})$$

Thus the Fourier transform of the time-shifted function has had its linear phase changed by  $\omega t_0$  relative to the unshifted Fourier transform.

*Product with sine.* For a time-domain function  $h(t) = f(t) \sin(\omega_c t)$ , its CFT can be shown to be

$$\tilde{h}(\omega) = \frac{\tilde{f}(\omega + \omega_c) - \tilde{f}(\omega - \omega_c)}{2i}, \quad (\text{A7})$$

allowing  $\tilde{h}(\omega)$  to be determined if  $\tilde{f}(\omega)$  is already known.

## Appendix B: Python code

The following Python routines use the numpy module "fft" to calculate the complex Fourier transform of the data "ydata", which is a function of the time variable "time". The complex spectrum as a function of positive and negative frequency is returned.

### 1. Forwards Fourier transform

```
def takeFFT(time,ydata,t0=0.0e-12):
    n = len(time)
    dt= abs(time[1]-time[0])

    ##### CALCULATE THE DFT USING NUMPY
    fftdata = n * fft.ifft(ydata,n=n)
    # Notes: - the ifft routine is used as it uses exp(i omega t).
    #         - numpy's ifft divides by n, so need to scale by n to be
    #         able to use this as the forward transform.

    ##### WORK OUT THE FREQUENCY ELEMENTS
    freq=fft.fftfreq(n=n, d=dt)
    # Notes: - freq runs from 0 -> f_max then -f_max -> -1/T,
    #         where f_max = 1/dt for time step "dt".

    ##### SHIFT THE DFT
    freq = fft.fftshift(freq)
```

```

fftdata = fft.fftshift(fftdata)
# Notes: - this makes the sequence run from -f_max to +f_max
#         so that it is symmetric about zero frequency, like the CFT

omega = 2*pi*freq

##### CORRECT THE DFT SO THAT IT AGREES WITH THE CFT
fftdata = fftdata * dt * exp(-i * omega * t0)
# Notes: - scaling factor "dt" needed for correct amplitude
#         - phase factor exp(-i * omega * t0) accounts for pulse
#         centred at time t0

return omega, fftdata

```

## 2. Inverse Fourier transform

```

def takeIFFT(omega,E_omega,t0=0.0e-12):
    delta_omega=omega[1]-omega[0]

    ##### WORK OUT Ek
    Ek = E_omega * exp(i*omega*t0)
    # Note: - input to DFT routine needs to use standard DFT with relative phase

    ##### SHIFT THE DFT
    Ek = fft.ifftshift(Ek)
    # Note: this puts the sequence back into the right order

    ##### WORK OUT THE TIME-DOMAIN FROM THE INVERSE TRANSFORM AND SCALE IT APPROPRIATELY
    Em = fft.fft(Ek)*delta_omega/(2*pi)
    # Here delta_omega/2 pi = 1/(n dt)

    return Em

```

## Appendix C: Detector response function

In the time-domain, the detected electro-optic signal  $S(t)$  is related to the THz electric field  $E(t)$  by  $S(t) = R(t) \otimes E(t)$ , where the influence of the detection crystal is captured by the convolution with the impulse response function,  $R(t)$ . In the frequency domain, via the convolution theorem the electro-optic signal is  $\tilde{S}(\omega) = \tilde{R}(\omega)\tilde{E}(\omega)$ , and hence we can determine the THz electric field from  $\tilde{E}(\omega) = \tilde{S}(\omega)/\tilde{R}(\omega)$ . We used the standard approach to determine  $\tilde{R}(\omega)$ : [32]

$$\tilde{R}(\omega) = r_{41}(\omega) \frac{e^{i\Delta k_P L} - 1.0}{i\Delta k_P L} \quad (\text{C1})$$

where  $\Delta k_P = \omega [\tilde{n}(\omega)/c - 1/v_g]$ , for a crystal with thickness  $L$ , THz complex refractive index  $\tilde{n}$ , and a probe beam with group velocity  $v_g$ . This response function includes the velocity mismatch between the THz and probe pulse as a result of the detection crystal's frequency-dependent refractive index [31], as well as the variation in the electro-optic coefficient  $r_{41}(\omega)$  with frequency [26]. Note that because  $\tilde{R}(\omega)$  is complex, and has a phase that is linear in the angular frequency, by the Fourier shift theorem dividing by  $\tilde{R}(\omega)$  changes the arrival time of the THz pulse in the time-domain. Here we accounted for this shift so that  $S(t)$  and  $E(t)$  both had  $t_e = 0$ , allowing a more straightforward

comparison of the temporal shapes before and after correcting for the detector’s response.

- 
- [1] James Lloyd-Hughes and Tae-In Jeon, “A review of the terahertz conductivity of bulk and nano-materials,” *J. Infrared Milli Terahz Waves* **33**, 871 (2012).
- [2] R Huber, A Brodschelm, F Tauser, and A Leitenstorfer, “Generation and field-resolved detection of femtosecond electromagnetic pulses tunable up to 41THz,” *Appl. Phys. Lett.* **76**, 3191–3193 (2000).
- [3] Dmitry Zimin, Matthew Weidman, Johannes Schötz, Matthias F. Kling, Vladislav S. Yakovlev, Ferenc Krausz, and Nicholas Karpowicz, “Petahertz-scale nonlinear photoconductive sampling in air,” *Optica* **8**, 586–590 (2021).
- [4] A. Herbst, K. Scheffter, M. M. Bidhendi, M. Kieker, A. Srivastava, and H. Fattahi, “Recent advances in petahertz electric field sampling,” *Journal of Physics B: Atomic, Molecular and Optical Physics* **55**, 172001 (2022).
- [5] Yoichi Kawada, Takashi Yasuda, and Hironori Takahashi, “Carrier envelope phase shifter for broadband terahertz pulses,” *Optics Letters* **41**, 986–989 (2016).
- [6] Nishtha Chopra and James Lloyd-Hughes, “Optimum optical designs for diffraction-limited terahertz spectroscopy and imaging systems using off-axis parabolic mirrors,” *J. Infrared Milli Terahz Waves* **44**, 981–997 (2023).
- [7] Petr Kužel, Maxim A. Khazan, and Jan Kroupa, “Spatiotemporal transformations of ultrashort terahertz pulses,” *J. Opt. Soc. Am. B* **16**, 1795–1800 (1999).
- [8] Jonas Allerbeck, Joel Kuttruff, Laric Bobzien, Lysander Huberich, Maxim Tsarev, and Bruno Schuler, “Efficient and continuous carrier-envelope phase control for terahertz lightwave-driven scanning probe microscopy,” *ACS Photonics* **10**, 3888–3895 (2023).
- [9] J. Lloyd-Hughes, P. M. Oppeneer, T. Pereira Dos Santos, A. Schleife, S. Meng, M. A. Sentef, M. Ruggenthaler, A. Rubio, I. Radu, M. Murnane, X. Shi, H. Kapteyn, B. Stadtmüller, K. M. Dani, F. H. Da Jornada, E. Prinz, M. Aeschlimann, R. L. Milot, M. Burdanova, J. Boland, T. Cocker, and F. Hegmann, “The 2021 ultrafast spectroscopic probes of condensed matter roadmap,” *J. Phys.: Cond. Matt.* **33**, 353001 (2021).
- [10] Peter Uhd Jepsen, “Phase retrieval in terahertz time-domain measurements: a “how to” tutorial,” *J. Infrared Milli Terahz Waves* **40**, 395–411 (2019).
- [11] E M Vartiainen, Y Ino, R Shimano, M Kuwata-Gonokami, Y P Svirko, and K E Peiponen, “Numerical phase correction method for terahertz time-domain reflection spectroscopy,” *J. Appl. Phys.* **96**, 4171–4175 (2004).
- [12] James Lloyd-Hughes, “[Github repository](#),” (2024).
- [13] Python Numpy; MathWorks Matlab.
- [14] C D W Mosley, M Failla, D Prabhakaran, and J Lloyd-Hughes, “Terahertz spectroscopy of anisotropic materials using beams with rotatable polarization,” *Scientific Reports* **7**, 12337 (2017).
- [15] Huiliang Ou, Rayko Ivanov Stantchev, Xuequan Chen, Thierry Blu, Mykhaylo Semtsiv, William Ted Masselink, Arturo Hernandez Serrano, Goncalo Costa, Jacob Young, Nishtha Chopra, James Lloyd-Hughes, and Emma MacPherson, “Simultaneous measurement of orthogonal terahertz fields via an emission multiplexing scheme,” *Opt. Expr.* **32**, 5567–5581 (2024).
- [16] Matthias C. Hoffmann, Ka-Lo Yeh, János Hebling, and Keith A. Nelson, “Efficient terahertz generation by optical rectification at 1035 nm,” *Opt. Expr.* **15**, 11706–11713 (2007).
- [17] H. Hirori, A. Doi, F. Blanchard, and K. Tanaka, “Single-cycle terahertz pulses with amplitudes exceeding 1 MV/cm generated by optical rectification in LiNbO<sub>3</sub>,” *Appl. Phys. Lett.* **98**, 091106 (2011).
- [18] T. Seifert, S. Jaiswal, U. Martens, J. Hannegan, L. Braun, P. Maldonado, F. Freimuth, A. Kronenberg, J. Henrizi, I. Radu, E. Beaurepaire, Y. Mokrousov, P. M. Oppeneer, M. Jourdan, G. Jakob, D. Turchinovich, L. M. Hayden, M. Wolf, M. Münzenberg, M. Kläui, and T. Kampfrath, “Efficient metallic spintronic emitters of ultrabroadband terahertz radiation,” *Nature Photonics* **10**, 483–488 (2016).
- [19] Connor D. W. Mosley, Daniel S. Lake, Darren M. Graham, Steven P. Jamison, Robert B. Appleby, Graeme Burt, and Morgan T. Hibberd, “Large-area periodically-poled lithium niobate wafer stacks optimized for high-energy narrowband terahertz generation,” *Opt. Expr.* **31**, 4041–4054 (2023).
- [20] Nan M. Froberg, Bin Bin Hu, Xi Cheng Zhang, and David H. Auston, “Terahertz radiation from a photoconducting antenna array,” *IEEE J. Quantum Electron.* **28**, 2291–2301 (1992).
- [21] A. S. Weling, B. B. Hu, N. M. Froberg, and D. H. Auston, “Generation of tunable narrow-band THz radiation from large aperture photoconducting antennas,” *Appl. Phys. Lett.* **64**, 137–139 (1994).
- [22] Stefano Barbieri, Marco Ravaro, Pierre Gellie, Giorgio Santarelli, Christophe Manquest, Carlo Sirtori, Suraj P. Khanna, Edmund H. Linfield, and A. Giles Davies, “Coherent sampling of active mode-locked terahertz quantum cascade lasers and frequency synthesis,” *Nature Photonics* **5**, 306–313 (2011).
- [23] B. Green, S. Kovalev, V. Asgekar, G. Geloni, U. Lehnert, T. Golz, M. Kuntzsch, C. Bauer, J. Hauser, J. Voigtlaender, B. Wustmann, I. Koesterke, M. Schwarz, M. Freitag, A. Arnold, J. Teichert, M. Justus, W. Seidel, C. Ilgner, N. Awari, D. Nicoletti, S. Kaiser, Y. Laplace, S. Rajasekaran, L. Zhang, S. Winnerl, H. Schneider, G. Schay, I. Lorincz, A. A. Rauscher, I. Radu, S. Mährlein, T. H. Kim, J. S. Lee, T. Kampfrath, S. Wall, J. Heberle, A. Malnasi-Csizmadia, A. Steiger, A. S. Möller, M. Helm, U. Schramm, T. Cowan, P. Michel, A. Cavalleri, A. S. Fisher, N. Stojanovic, and M. Gensch, “High-Field High-Repetition-Rate Sources for the Coherent THz Control of Matter,” *Scientific Reports* **6**, 1–9 (2016).

- [24] Saima Ahmed, Peter Hamm, and Janne Savolainen, “The effect of the Gouy phase in optical-pump-THz-probe spectroscopy,” *Opt. Expr.* **22**, 4256–4266 (2014).
- [25] Matthias Knorr, Philipp Steinleitner, Jürgen Raab, Imke Gronwald, Philipp Merkl, Christoph Lange, and Rupert Huber, “Ultrabroadband etalon-free detection of infrared transients by van-der-Waals contacted sub-10- $\mu\text{m}$  gas detectors,” *Optics Express* **26**, 19059–19066 (2018).
- [26] A Leitenstorfer, S Hunsche, J Shah, M C Nuss, and W H Knox, “Detectors and sources for ultrabroadband electro-optic sampling: Experiment and theory,” *Appl. Phys. Lett.* **74**, 1516–1518 (1999).
- [27] C Kübler, R Huber, S Tübel, and A Leitenstorfer, “Ultrabroadband detection of multi-terahertz field transients with gas electro-optic sensors: Approaching the near infrared,” *Appl. Phys. Lett.* **85**, 3360–3362 (2004).
- [28] E. W. Snedden, D. A. Walsh, and S. P. Jamison, “Revealing carrier-envelope phase through frequency mixing and interference in frequency resolved optical gating,” *Optics Express* **23**, 8507–8518 (2015).
- [29] Zhen Zhang, Yanping Chen, Zhelin Zhang, Tianhao Xia, Jiayang Zhang, Zhengming Sheng, and Jie Zhang, “Phase evolution of terahertz radiation from femtosecond laser-induced air plasma,” *Optics Letters* **45**, 1966–1969 (2020).
- [30] Nishtha Chopra, Justas Deveikis, and James Lloyd-Hughes, “Active THz beam shaping using a one-dimensional array of photoconductive emitters,” *Appl. Phys. Lett.* **122**, 061102 (2023).
- [31] G Gallot, J Q Zhang, R W McGowan, Tae-In Jeon, and D Grischkowsky, “Measurements of the THz absorption and dispersion of ZnTe and their relevance to the electro-optic detection of THz radiation,” *Appl. Phys. Lett.* **74**, 3450–3452 (1999).
- [32] S. Casalbuoni, H. Scharb, B. Schmidt, P. Schmüser, B. Steffen, and A. Winter, “Numerical studies on the electro-optic detection of femtosecond electron bunches,” *Phys. Rev. ST Accel. Beams* **11**, 072802 (2008).
- [33] Alfred Leitenstorfer, Andrey S. Moskalenko, Tobias Kampfrath, Junichiro Kono, Enrique Castro-Camus, Kun Peng, Naser Qureshi, Dmitry Turchinovich, Koichiro Tanaka, Andrea G. Markelz, Martina Havenith, Cameron Hough, Hannah J. Joyce, Willie J. Padilla, Binbin Zhou, Ki Yong Kim, Xi Cheng Zhang, Peter Uhd Jepsen, Sukhdeep Dhillon, Miriam Vitiello, Edmund Linfield, A. Giles Davies, Matthias C. Hoffmann, Roger Lewis, Masayoshi Tonouchi, Pernille Klarskov, Tom S. Seifert, Yaroslav A. Gerasimenko, Dragan Mihailovic, Rupert Huber, Jessica L. Boland, Oleg Mitrofanov, Paul Dean, Brian N. Ellison, Peter G. Huggard, Simon P. Rea, Christopher Walker, David T. Leisawitz, Jian Rong Gao, Chong Li, Qin Chen, Gintaras Valušis, Vincent P. Wallace, Emma Pickwell-MacPherson, Xiaobang Shang, Jeffrey Hesler, Nick Ridler, Cyril C. Renaud, Ingmar Kallfass, Tadao Nagatsuma, J. Axel Zeitler, Don Arnone, Michael B. Johnston, and John Cunningham, “The 2023 terahertz science and technology roadmap,” *Journal of Physics D: Applied Physics* **56**, 223001 (2023).
- [34] Paul M. Donaldson, “Spectrophotometric concentration analysis without molar absorption coefficients by two-dimensional-infrared and fourier transform infrared spectroscopy,” *Analytical Chemistry* **94**, 17988–17999 (2022).